

## CHANDRA EVIDENCE FOR A FLATTENED, TRIAXIAL DARK MATTER HALO IN THE ELLIPTICAL GALAXY NGC 720

DAVID A. BUOTE<sup>1</sup>, TESLA E. JELTEMA<sup>2</sup>, CLAUDE R. CANIZARES<sup>2</sup>, & GORDON P. GARMIRE<sup>3</sup>  
*Accepted for Publication in The Astrophysical Journal*

### ABSTRACT

We present an analysis of a *Chandra* ACIS-S observation of the elliptical galaxy NGC 720 to verify the existence of a dark matter halo and to measure its ellipticity. The ACIS-S3 image reveals over 60 point sources distributed throughout the field, most of which were undetected and therefore unaccounted for in previous X-ray studies. For semi-major axes  $a \lesssim 150''$  ( $18.2h_{70}^{-1}$  kpc) the ellipticity of the diffuse X-ray emission is consistent with a constant value,  $\epsilon_x \approx 0.15$ , which is systematically less than the values 0.2-0.3 obtained from previous *ROSAT* PSPC and HRI observations because of the unresolved point sources contaminating the *ROSAT* values. The *Chandra* data confirm the magnitude of the  $\sim 20^\circ$  position angle (PA) twist discovered by *ROSAT* over this region. However, the twist in the *Chandra* data is more gradual and occurs at smaller  $a$  also because of the point sources contaminating the *ROSAT* values. For  $a \gtrsim 150''$  out to  $a = 185''$  ( $22.4h_{70}^{-1}$  kpc), which is near the edge of the S3 CCD,  $\epsilon_x$  and PA diverge from their values at smaller  $a$ . Possible origins of this behavior at the largest  $a$  are discussed.

Overall the ellipticities and PA twist for  $a \lesssim 150''$  can be explained by the triaxial mass model of NGC 720 published by Romanowsky & Kochanek (which could not produce the abrupt PA twist in the *ROSAT* HRI data). Since the optical image displays no substantial isophote twisting, the X-ray PA twist requires a massive dark matter halo if the hot gas is in hydrostatic equilibrium. Furthermore, the values of  $\epsilon_x$  obtained by *Chandra* are too large to be explained if the gravitating mass follows the optical light ( $M \propto L_*$ ) irrespective of the PA twist: The  $M \propto L_*$  hypothesis is inconsistent with the *Chandra* ellipticities at the 96% confidence level assuming oblate symmetry and at the 98% confidence level for prolate symmetry. Thus, both the PA twist and the ellipticities of the *Chandra* image imply the existence of dark matter independent of the temperature profile of the gas. This geometric evidence for dark matter cannot be explained by alternative gravity theories such as the Modification of Newtonian Dynamics (MOND).

To constrain the ellipticity of the dark matter halo we considered both oblate and prolate spheroidal mass models to bracket the full range of (projected) ellipticities of a triaxial ellipsoid. The dark matter density model,  $\rho \propto (a_s^2 + a^2)^{-1}$ , provides the best fit to the data and gives ellipticities and  $1\sigma$  errors of  $\epsilon = 0.37 \pm 0.03$  for oblate and  $\epsilon = 0.36 \pm 0.02$  for prolate models. Navarro-Frenk-White (NFW) and Hernquist models give similar ellipticities for the dark matter. These moderate ellipticities for the dark halo are inconsistent with both the nearly spherical halos predicted if the dark matter is self-interacting and with the highly flattened halos predicted if the dark matter is cold molecular gas. These ellipticities may also be too large to be explained by warm dark matter, but are consistent with galaxy-sized halos formed in the currently popular  $\Lambda$ CDM paradigm.

*Subject headings:* X-rays: galaxies – galaxies: halos – galaxies: formation – galaxies: elliptical and lenticular, cD – galaxies: individual: NGC 720 – dark matter

### 1. INTRODUCTION

It is now almost 20 years that the “Cold Dark Matter” paradigm (CDM), in which most of the matter in the universe is assumed to be collisionless dark matter, has been regarded as the standard cosmological model of the formation of structure in the universe. The CDM model (and particularly its variant  $\Lambda$ CDM) has achieved many successes in describing current observations, especially with regard to the cosmic microwave background radiation and the large-scale clustering properties of galaxies (e.g., Rees 2000). Recently, however, many have drawn attention to the problems  $\Lambda$ CDM has describing structure on galaxy scales (e.g., Sellwood & Kosowsky 2002b).

One problem with CDM is that it predicts that all galaxies, including elliptical galaxies, should possess massive dark matter halos. But definitive evidence for such halos in isolated elliptical galaxies has proven difficult to establish. Stellar dynamical analyses have made significant progress limiting the uncertainties on the radial mass profile in Es due to velocity dispersion anisotropy (e.g., de Zeeuw 1997; Gerhard 2002), but a recent study by Baes & Dejonghe (2001) argues that interstellar dust in Es renders such mass determinations unreliable. Gravitational lensing studies have the potential to provide important constraints on the mass distributions in elliptical galaxies from statistical analysis of the weak shear fields of many galaxies (e.g., Natarajan & Refregier 2000). Statistical av-

<sup>1</sup> Department of Physics and Astronomy, University of California at Irvine, 4129 Frederick Reines Hall, Irvine, CA 92697-4575

<sup>2</sup> Center for Space Research and Department of Physics, Massachusetts Institute of Technology 37-241, 77 Massachusetts Avenue, Cambridge, MA 02139

<sup>3</sup> The Pennsylvania State University, 525 Davey Lab, University Park, PA 16802

eraging of the properties of strong lenses has not yet provided clear evidence for dark matter in isolated Es (e.g., Keeton et al. 1998).

There is evidence for dark matter in the outer halos ( $\gtrsim 100$  kpc) of elliptical galaxies obtained from kinematic tracers such as globular clusters, though for the few objects studied the inferred masses imply a surrounding group or cluster (e.g., in NGC 4472, Zepf 2002). Accurate constraints on the radial temperature profiles of hot gas obtained by *ROSAT* X-ray observations have indicated substantial amounts of dark matter for elliptical galaxies in the centers of groups (e.g., NGC 1399, Jones et al. 1997) and clusters (e.g., M87, Nulsen & Bohringer 1995). But because they are fainter in X-rays, *ROSAT* (and *Einstein*, Fabbiano 1989) did not provide temperature profiles of sufficient accuracy to clearly demonstrate the need for dark matter in isolated Es.

It is clear that the evidence for dark matter in isolated elliptical galaxies just mentioned is not extensive, and even in disk galaxies the case for dark matter is not considered to be as strong as it once was (e.g., Evans 2002). Even for those galaxies where dark matter is suggested on the basis of standard Newtonian gravity, Sellwood & Kosowsky (2002a) argue that all such evidence for dark matter cannot be distinguished from general modified gravity theories, such as the Modification of Newtonian Dynamics (MOND), proposed by Milgrom (1983c,a,b).

A powerful test for dark matter that can distinguish dark matter from MOND in isolated Es is the ‘‘Geometric Test for Dark Matter’’ we introduced previously (Buote & Canizares 1994, 1996b, 1998a). The Geometric Test is a comparison between the ellipticities and orientations of the observed X-ray isophotes with those expected if the gravitating mass traces the same shape as the stellar light. Applying this Geometric Test to the ellipticities of the *ROSAT* data of two isolated Es and one isolated S0 galaxy, we found strong evidence for dark matter for the E4 galaxy NGC 720 (99% conf.) and marginal evidence for the S0 galaxy NGC 1332 (90% conf.) and the E4 galaxy NGC 3923 (80%-85% conf.) – see Buote & Canizares (1998a) for a review. The *ROSAT* data of NGC 720 also displayed an X-ray position angle twist. But this twist could not be explained with triaxial dark matter models (Buote & Canizares 1996a; Romanowsky & Kochanek 1998) which cast some doubt on whether the X-ray emission indeed traces the potential in NGC 720. And since the evidence for dark matter in NGC 1332 and NGC 3923 is marginal, higher quality observations of these systems are required to assess more definitively the existence of dark matter halos.

For the galaxies mentioned above we inferred from the *ROSAT* observations that the dark matter ellipticities range from approximately 0.4 – 0.6 with some indication (particularly in NGC 720) that the mass is flatter than the stellar distribution. These moderate ellipticities provide important constraints on competing models for the dark matter, some of which predict spherical halos (Spergel & Steinhardt 2000), highly flattened halos (Pfenniger et al. 1994), and moderately flattened halos (e.g., Bullock 2002).

Owing to the small number of measurements of the flattening of dark halos (e.g., Merrifield 2002; Sackett 1996), and that such previous measurements are of limited accuracy, the different predictions for halo shapes have not yet been given a definitive test.

We have obtained a high-resolution *Chandra* observation of NGC 720 to reexamine the existence of a dark matter halo via the Geometric Test and to measure its flattening. A major issue to be addressed is the effect of discrete sources, such as have been found in large quantities for early-type galaxies with *Chandra* (e.g., Sarazin et al. 2000), on the conclusions drawn from lower resolution *ROSAT* data. Although calculating triaxial models is beyond the scope of this paper, we will also measure the position angles of the X-ray isophotes and compare them to the previously published triaxial model of Romanowsky & Kochanek (1998). We assume a distance of 25 Mpc to NGC 720 for  $H_0 = 70h_{70}$  km s $^{-1}$  Mpc $^{-1}$  (and  $\Omega_0 = 0.3$ ) in which case  $1'' = 0.12$  kpc.

The paper is organized as follows. We discuss the data preparation in §2. The treatment of point sources and the measurement of the X-ray ellipticities, position angles, and radial profile are discussed in §3. The Geometric Test for dark matter is performed in §4. We examine the *Chandra* constraints on the temperature profile in §5 and the ellipticity of the dark matter in §6. Finally, in §7 we present our conclusions.

## 2. OBSERVATIONS AND DATA REDUCTION

NGC 720 was observed with the ACIS-S3 camera for  $\approx 40$  ks during AO-1 as part of the guaranteed-time-observer program (PI Garmire). The events list was corrected for charge-transfer inefficiency according to Townsley et al. (2002), and only events characterized by the standard ASCA grades<sup>4</sup> were used. The standard CIAO<sup>5</sup> software (version 2.2.1) was used for most of the subsequent data preparation.

Since the diffuse X-ray emission of NGC 720 fills the entire S3 chip, we used the standard background templates<sup>6</sup> to model the background. When attempting to use the LC\_CLEAN script to clean the source events list of flares with the same screening criteria as the background templates, only 12 ks of data remained. Examination of the original light curve reveals only one significant flare ( $\sim 6$  ks worth of data) near the beginning of the observation, but the light curve does gently rise and fall during the rest of the observation so that most of the data does not lie within the standard 3-sigma clip. Consequently, we excluded only the obvious flare leaving a total exposure of 34.4 ks.

Because the quiescent background can vary typically by  $\sim 10\%$  between observations, and we do not use exactly the same screening criteria as the templates, it is necessary to normalize the background templates to match the NGC 720 observation. Since NGC 720 has a gas temperature  $\sim 0.6$  keV there is little emission from hot gas for energies  $> 5$  keV. Consequently, we normalized the S3 background template by comparing source and background counts in the 5-10 keV band extracted from regions near the edges of the S3 field.

<sup>4</sup> <http://cxc.harvard.edu/udocs/docs/docs.html>

<sup>5</sup> <http://cxc.harvard.edu/ciao/>

<sup>6</sup> <http://cxc.harvard.edu/cal>

We binned the cleaned S3 events lists for the source and background into images of  $1'' \times 1''$  pixels (actually  $0.984'' \times 0.984''$  pixels, but we shall round off throughout the paper). Since background dominates at high energies we selected events with energies 0.3-3 keV. Likely problems with the spectral calibration near the low end of the bandpass (see §5) are not important for the imaging analysis.

Although vignetting is a small effect within  $\approx 3'$  of the aim point of the S3 where our analysis is concentrated, we explored the viability of using an exposure map to flatten the image. The inherent difficulty in constructing a single exposure map for the image of a diffuse source for instruments like ACIS has been discussed by Davis (2001) and Houck<sup>7</sup>. Since, however, the diffuse gas of NGC 720 is remarkably isothermal (see §5) we are able to construct a well-defined “weighted” exposure map following the procedure on the CIAO website. (Note we find no tangible differences in any results mentioned below if instead we use a monochromatic exposure map evaluated at 0.77 keV which is the peak of the counts spectrum.)

Unfortunately, the current method for flat-fielding images introduces spurious features along node boundaries where the intrinsic exposure is small relative to the rest of the CCD. When the exposure map is divided into the raw image to create an exposure-corrected image, regions of relatively low exposure (e.g., node boundaries, bad columns, and edges) require large corrections. Any intrinsic errors in the exposure map in these regions, and any noise in the data, will be amplified as a result.

For NGC 720 we find that dividing by the exposure map amplifies the linear distortion along the node 1-2 boundary that reaches within  $\approx 30''$  of the center of NGC 720. Ellipticities and position angles computed between radii of  $\sim 30'' - 60''$  are systematically lower by 20%–30% with respect to their values obtained from the un-flattened image. We emphasize that in the raw image the linear distortion is very faint and very difficult to see, and imperceptible in the smoothed image displayed in Figure 1; i.e., this feature has negligible effect on the ellipticities and position angles considering the statistical uncertainties on these quantities (§3.2.2). Consequently, since we have a case where “the cure is worse than the disease”, when computing ellipticities and position angles we do not use the exposure-corrected image. But since this non-circular, low-surface brightness feature amplified by the exposure map has no perceptible effect on the azimuthally averaged radial profile, we do use the exposure-corrected image to account for the small effects of (large-scale) telescopic vignetting for analysis of the image radial profile.

### 3. IMAGE ANALYSIS

In Figure 1 we display the adaptively smoothed S3 image of NGC 720 within a radius of  $150''$  of the galaxy center with some isophotal contours overlaid. (This smoothing is done only for display purposes. All analysis discussed below is performed on the unsmoothed image; cf. Figure 1 of Jeltema et al. 2002). The most striking difference between the *Chandra* and *ROSAT* images (e.g., Buote & Canizares 1998a) is the large number of point sources clearly detected by *Chandra*. Many of these sources are located within  $1'$

of the galaxy center.

The morphology of the diffuse emission within  $\sim 100''$  of the galaxy center is similar to that described for previous *ROSAT* observations. The isophotes are moderately flattened and the orientations of the outer isophotes appear to be tilted with respect to the innermost regions. But caution must be exercised when viewing this adaptively smoothed image since small-scale features in the diffuse emission have low statistical significance (especially apparent wiggles in the isophotes). Below we shall quantify the morphology of the diffuse emission using moments of the image.

#### 3.1. Removal of Point Sources

Before we can analyze the properties of the diffuse emission we must remove the point sources. (Analysis of the properties of these sources is presented in a companion paper – Jeltema et al. 2002.) However, it is insufficient only to remove the sources since holes in the image still affect significantly quantities like the ellipticity that are derived from second (or higher) moments of the image. To obtain reliable measurements of the ellipticity and position angle throughout the source-free image it is necessary to replace each embedded source with a faithful representation of the local diffuse X-ray emission surrounding the source.

We located point sources with the CIAO task WAVDETECT (a wavelet detection algorithm) using the default parameter settings. A total of 64 sources were detected over the entire S3 field excluding the center of NGC 720. These include the 41 sources within  $2.5'$  of the galaxy center discussed by Jeltema et al. (2002).

To remove these sources and “fill” in the holes with diffuse emission we used the CIAO task DMFILTH. This task takes as input source and background region definitions. The counts within the source regions are replaced with values sampled from the background regions. Within  $\sim 3'$  of the galaxy center we defined the source extraction regions as circles of radius  $2''$ . The corresponding concentric background regions all have radius  $4''$ . The average background counts in each region was determined by the polynomial method in DMFILTH. Since in several cases the background region of one source overlapped another (especially within  $\sim 30''$  of the galaxy center) we iterated runs of DMFILTH using the cleaned images of previous runs as input to subsequent runs. We found that the results converged after only three runs.

For radii larger than  $\sim 30''$  we found that DMFILTH performed well. In this context “well” means that the measured ellipticity and position angle are smoothly varying functions of radius; i.e., at the radius of a filled-in source the ellipticity and position angle do not deviate substantially from values obtained at adjacent source-free radii. Unfortunately, for radii  $\lesssim 30''$  we found that the ellipticity and position angle did jump “discontinuously” near some filled-in sources, especially at the smallest radii  $\lesssim 15''$  where source background-region overlap (as noted above) is most pronounced. (Note that such jumps, by accident, are not apparent for the ellipticity and position angle at the particular radii  $\lesssim 30''$  plotted below.)

At small radii the relative effect of the sources on derived surface brightness parameters is necessarily greater

<sup>7</sup> see [http://cxc.harvard.edu/ciao/documents\\_manuals.html](http://cxc.harvard.edu/ciao/documents_manuals.html)

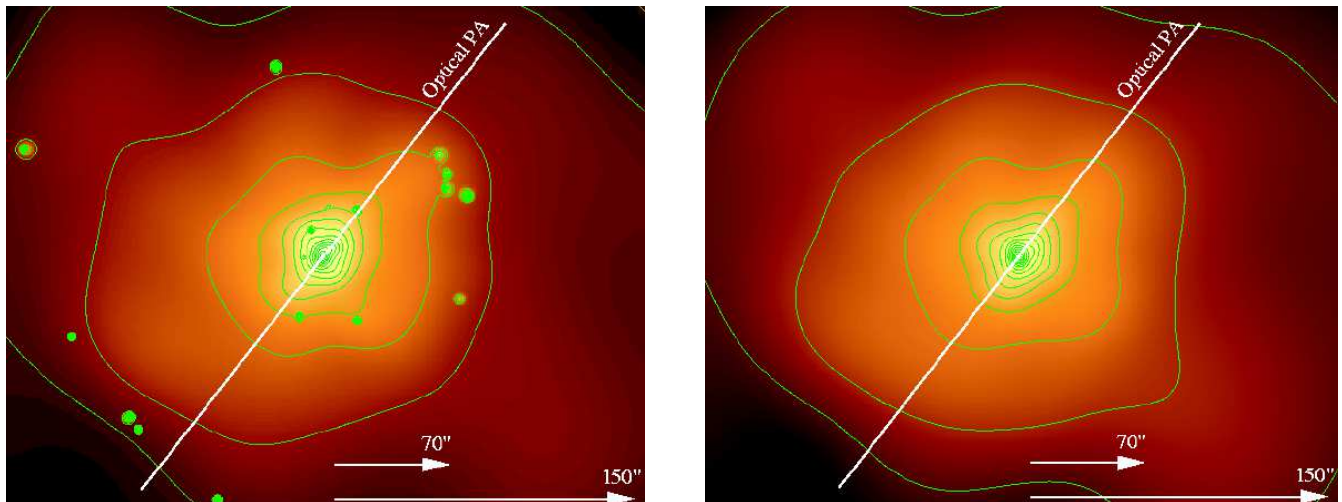


FIG. 1.— (Left) False-color ACIS-S3 image of NGC 720 in the 0.3-3 keV band. The image has been adaptively smoothed using the CIAO task CSMOOTH with default parameters. No exposure-map correction or background subtraction has been applied. Contours are spaced according to the square root of the intensity. (Right) Same image except the point sources have been removed. The contour levels are the same as the original image. Each image is oriented so that celestial N is up and E is to the left.

because the area of the source becomes increasingly more significant relative to  $r^2$ . It is likely that at such small radii the approach of simply filling in the source region with a spatially uniform count distribution does not faithfully (enough) represent the shape the local diffuse emission. We defer consideration of more sophisticated source-replacement algorithms to a future study. In our analyses below we treat the region  $r \lesssim 30''$  with caution.

As should be expected, residual source-replacement effects in these inner regions are much less important for the radial profile. We shall therefore use the whole image for construction and analysis of the radial profile.

### 3.2. $\epsilon_x$ and PA

#### 3.2.1. Method

The flattening of the X-ray isophotes is of central importance to our study of the flattening and concentration of the total gravitating matter in NGC 720. The standard parameter used to denote the flattening of an individual isophote is the ellipticity,  $1 - b/a$ , where  $a$  is the semi-major axis and  $b$  is the semi-minor axis. However, fitting perfect ellipses to the X-ray isophotes is not necessarily justified since the isopotential surfaces generated by an elliptical mass distribution are not perfect ellipsoids. In addition, over most of the X-ray image the surface brightness of the diffuse gas is  $\lesssim 1$  counts per pixel. This condition requires that relatively large areas (in excess of a single-pixel width isophote) must be averaged over to obtain interesting constraints on the image flattening.

We quantify the image flattening using the method described by Carter & Metcalfe (1980) and implemented in our previous study of the *ROSAT* image of NGC 720 (e.g. Buote & Canizares 1994). This iterative method is equivalent to computing the (two-dimensional) principal moments of inertia within an elliptical region. The ellipticity,  $\epsilon_x$ , is defined by the square root of the ratio of the principal moments, and the position angle, PA, is defined by the orientation of the larger principal moment. If these moments are computed within an elliptical region where the image is perfectly elliptical with constant ellipticity and

orientation, then  $\epsilon_x$  represents a true ellipticity and PA is the true orientation of the major axis. If the image is not perfectly elliptical within this region, then  $\epsilon_x$  and PA are average values weighted heavily toward the edge of the region; i.e.,  $\epsilon_x$  provides a useful measure of image flattening which does not assume the image to be perfectly elliptical.

Following our previous studies we compute  $\epsilon_x(a)$  using all image pixels interior to the ellipse defined at  $a$  (obtained via iteration). We did investigate using elliptical annuli to provide a more direct measurement of the variation of  $\epsilon_x$  with  $a$ . Unfortunately, because of the low counts per pixel noted above the radial fluctuations of  $\epsilon_x$ , PA, and centroid were considerably larger when using elliptical annuli.

We estimate uncertainties on  $\epsilon_x$  and PA using a Monte Carlo procedure. The counts in each pixel are randomized assuming poisson statistics. Then  $\epsilon_x$  and PA are computed precisely as done for the original image. After performing 100 such realizations and corresponding “measurements” of the image we compute the standard deviations of  $\epsilon_x$  and PA at each  $a$  for the 100 runs. We take these standard deviations to be the  $1\sigma$  errors.

We have computed  $\epsilon_x$  and PA out to  $a = 185''$  from the *Chandra* image such that the background-subtracted counts in each aperture increase by  $\approx 500$  for each  $a$ . (The edge of the S3 chip corresponds to  $r \approx 215''$ .) Because we use all image pixels interior to  $a$  to compute  $\epsilon_x$  and PA, their values computed for a given  $a$  are correlated with values computed at adjacent inner  $a$ . This means that the error bars on  $\epsilon_x$  and PA for adjacent  $a$  are not fully independent. But we emphasize that these quantities, being derived from second moments of the image, are weighted heavily by the pixels near  $a$ .

#### 3.2.2. Results

In Figure 2 we show  $\epsilon_x$  and PA computed from the *Chandra* image before and after removing the point sources. (Note the error bars for values computed from the image with sources are not shown for clarity but are of similar magnitude to those obtained from the source-free image.) For the image with point sources, within  $a \lesssim 80''$   $\epsilon_x$  varies

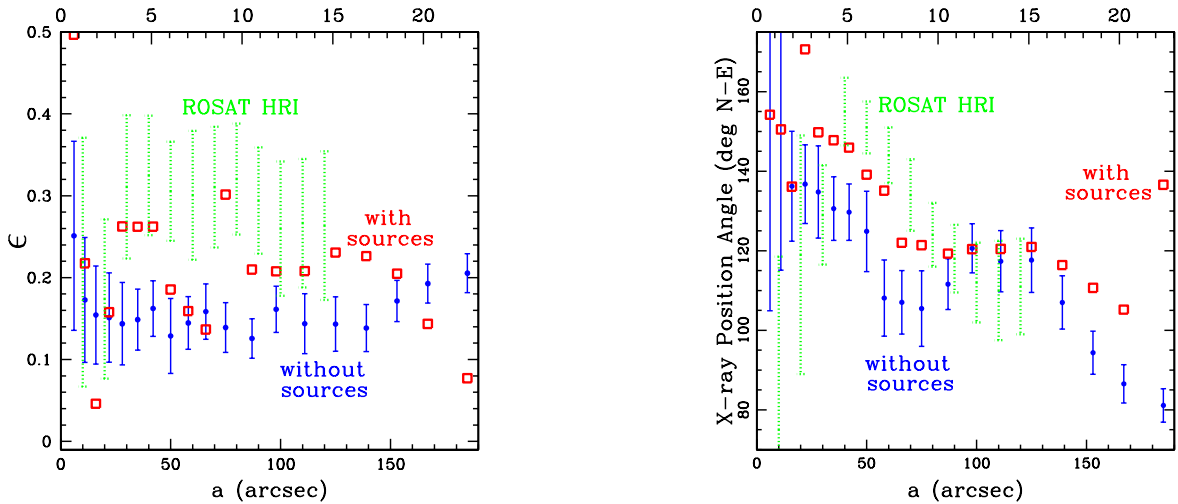


FIG. 2.— (Left panel)  $\epsilon_x$  as a function of semi-major axis computed from the *Chandra* image with point source removed (circles and error bars; blue). The (red) boxes are the values of  $\epsilon_x$  obtained from the image which includes the point sources. The (green) dotted error bars are the values obtained with the ROSAT HRI (Buote & Canizares 1996a) (Right panel) PA as a function of  $a$  computed from the *Chandra* image with point sources removed (circles and error bars; blue). The (red) boxes are the values of  $\epsilon_x$  obtained from the image which includes the point sources. Note that because we use all image pixels interior to  $a$  to compute  $\epsilon_x$  and PA, the values and the error bars for adjacent  $a$  are not independent. We express  $a$  in kpc on the top axis.

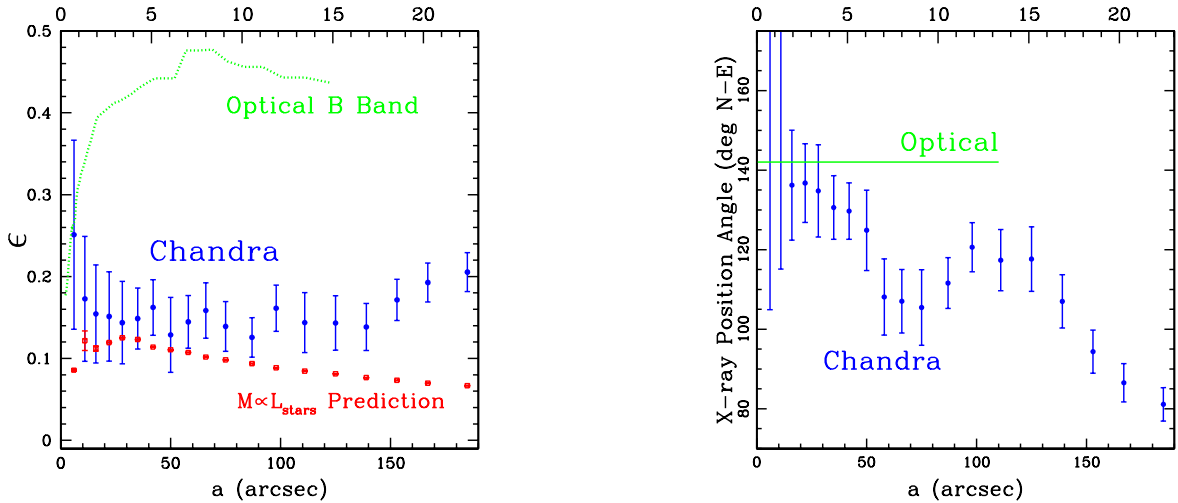


FIG. 3.— (Left panel)  $\epsilon_x$  as a function of semi-major axis computed from the source-free *Chandra* image (circles and error bars; blue). The optical B-band ellipticity is indicated by the (green) dashed line (see §4.2). The values of  $\epsilon_x$  expected for a model where the gravitating mass follows the optical light is shown by the (red) squares; i.e., the oblate  $M \propto L_*$  model mentioned in the text. (Right panel) PA as a function of  $a$  computed from the source-free *Chandra* image (circles and error bars; blue). The optical B-band value (green) is also shown. We express  $a$  in kpc on the top axis.

wildly with  $a$  then settles down to  $\epsilon_x \approx 0.2$  until it declines for  $a \gtrsim 150''$ . This erratic behavior is a stark contrast to the slowly varying values of  $\epsilon_x$  computed from the source-free image. *We interpret this result as a strong affirmation of our success at removing and replacing the point sources over this range in  $a$  for the purpose of computing  $\epsilon_x$ .*

The PA generally does not exhibit such dramatic variations with  $a$  in either case, though the PA values computed from the image with sources (for the most part) systematically exceed those computed from the source-free image by  $\sim 10^\circ$ . This relative similarity between the PAs computed from the raw and source-free images coupled with the lack of strong fluctuations with  $a$  suggest that PA is less sensitive than is  $\epsilon_x$  to contaminating point sources. However, with the present data we cannot rule out the possibility that PA is more sensitive than  $\epsilon_x$  to contaminating point

sources and is therefore only slightly affected by our attempt to exclude and replace the sources. Since the values of  $\epsilon_x$  and PA are necessarily intertwined, and we are confident of the success in computing  $\epsilon_x$ , we do not believe the PA values computed from the source-free image are still substantially affected by embedded point sources. Nevertheless, to be conservative we shall address below the need for dark matter in NGC 720 using  $\epsilon_x$  and PA separately.

Let us focus on the source-free image (Figure 3). As explained above in §3.1 the best-fitting values of  $\epsilon_x$  and PA computed within  $a \lesssim 30''$  must be considered tentative because of residual source-replacement errors. Nevertheless, certain trends in these data appear to be robust. First, for small  $a$  we have,  $\epsilon_x \approx 0.2 - 0.3$ , consistent with the optical isophotes in this region within the relatively large estimated errors. Second, the position angle is consistent

with the optical value,  $PA \approx 142^\circ$  (N-E), for  $a \lesssim 30''$ .

For  $30'' \lesssim a \lesssim 150''$  the ellipticity is consistent with a constant value,  $\epsilon_x \approx 0.15$ . This value is notably smaller than the best-fitting values of  $\approx 0.20 - 0.30$  obtained with the *ROSAT* PSPC and HRI (Buote & Canizares 1994, 1996a, 1998a) between  $30'' \lesssim a \lesssim 110''$ ; the HRI values are reproduced in Figure 2. The overall consistency of the  $\epsilon_x$  values obtained from the *ROSAT* image and *Chandra* image with sources demonstrates that the embedded point sources are responsible for the *ROSAT* values. The most important are the group of point sources located  $\approx 70''$  to the NW of the galaxy center. These sources were not identified and removed from the *ROSAT* images (and evaded detection from our symmetry tests because they are located near the X-ray major axis). Note that the source-free *Chandra*  $\epsilon_x$  values are smaller than obtained from the HRI for  $50'' \lesssim a \lesssim 70''$ . This discrepancy is not resolved by simply degrading the *Chandra* data by smoothing it with the HRI PSF. We have not definitively identified the origin of this discrepancy, but we suspect it is associated with the different flux sensitivities of the HRI and ACIS; i.e., flat spectrum point sources will be more prominent with respect to the diffuse hot gas in the ACIS data.

The magnitude of the PA twist discovered by *ROSAT* is confirmed by the source-free *Chandra* data, but the precise radial variation of PA is different because of the unresolved point sources present in the *ROSAT* data. For  $80'' \lesssim a \lesssim 150''$  the position angles,  $PA \approx 110^\circ$ , measured by *Chandra* are consistent with the *ROSAT* values. However, for  $a \sim 60''$  the *ROSAT* HRI PA jumps to a value  $PA \approx 140^\circ$  whereas the source-free *Chandra* PA increases more gradually from  $PA \approx 120^\circ$  to  $PA \approx 135^\circ$  for decreasing  $a$  within  $a \lesssim 60''$ . The similarity of the PA values obtained for the *Chandra* image with sources and the HRI demonstrate that the embedded point sources are responsible for the inflated PA values. The key point sources for these inflated PA values are located  $\sim 45''$  to the SW of the galaxy center along the minor axis (see Figure 1 above and Figure 1 of Jeltema et al. 2002).

At large radius ( $150'' \lesssim a \lesssim 180''$ )  $\epsilon_x$  increases steadily to a value of  $\approx 0.20$  while the position angle decreases to a value of  $\approx 80^\circ$ . These changes are highly significant statistically and are obvious upon inspection of the smoothed image displayed in Figure 1. For  $a \gtrsim 120''$  the PSPC and *Chandra* values of  $\epsilon_x$  agree within errors. This suggests that the effect of unresolved sources on  $\epsilon_x$  is less important at large radius as might be expected since the PSF FWHM compared to  $a$  decreases with increasing  $a$ . However, the PA measured by the PSPC at large radius does not appear to twist so much as seen in the *Chandra* data: PSPC PA values are  $102^\circ \pm 9^\circ$  at  $a = 150''$  and  $107^\circ \pm 5^\circ$  at  $a = 225''$  (Buote & Canizares 1994).

The origin of this *Chandra-ROSAT* PA discrepancy at large radius is unclear, but we would tend to believe the *Chandra* values because of the issue of point sources in the *ROSAT* data. It must be acknowledged, however, that since the edge of the S3 chip is at  $a \approx 215''$  there could be problems with flat-fielding which we think unlikely based on our own investigations with exposure maps in this region. It is probably necessary to use the wide-field XMM EPIC CCDs to resolve this issue.

### 3.3. Radial Profile

The radial profile ( $\Sigma_x(r)$ ) is the final property derived from the X-ray image that is required to constrain the shape of the gravitating matter distribution. We define the image radial profile by first summing the background-subtracted counts in concentric circular annuli with radii determined by the semi-major axes used to compute  $\epsilon_x$  and PA (§3.2.2). Then dividing the counts in each annulus by the area of the annulus we arrive at the radial profile. The center of each annulus is the same and is taken to be the centroid computed within a circle of radius  $20''$  placed initially at X-ray peak. (The centroid varies by  $\lesssim 4''$  for  $r \leq 185''$ .) There are  $\approx 12000$  background-subtracted counts within  $r = 185''$ .

We plot  $\Sigma_x(r)$  in Figure 4. The radial profile is quite smooth over the entire range investigated. The somewhat bumpy HRI profile (Buote & Canizares 1996a) within  $r \lesssim 30''$  can be attributed to noise and to the point sources detected in that region by *Chandra*. Fitting the *Chandra* profile with a  $\beta$  model yields  $r_c \approx 4.6''$  and  $\beta \approx 0.42$  in agreement with the HRI values. The  $\beta$  model is an excellent qualitative (i.e., visual) fit to  $\Sigma_x(r)$ , but because the error bars are very small the formal quality of the fit is rather poor:  $\chi^2 = 44.3$  for 16 degrees of freedom (dof). The most important fit residuals occur in the inner bins. These residuals are small when expressed as a ratio of data to model (i.e.,  $< 10\%$ ), but are relatively large when expressed in terms of a  $\chi^2$  difference between data and model. If, for example, the inner 3 bins are excluded ( $r \lesssim 16''$ ) we obtain  $\chi^2 = 24.9$  for 13 dof.

## 4. GEOMETRIC TEST FOR DARK MATTER

### 4.1. Basic Idea and Assumptions

Previously, we have shown that it is possible to test the hypothesis that the gravitating mass traces the stellar light using only the X-ray imaging data of the diffuse hot gas – no knowledge of the value of the gas temperature or a possible spatial temperature gradient is required (Buote & Canizares 1994, 1996b, 1998a). The key assumptions are that the hot gas is single-phase and in hydrostatic equilibrium. If these conditions hold, then the gas volume emissivity,  $j_x$ , and the potential of the gravitating matter,  $\Phi$ , must have identical shapes in three-dimensional space (“X-Ray Shape Theorem”); i.e., *in 3D the surfaces of constant  $j_x$  are surfaces of constant  $\Phi$  independent of the temperature profile of the gas.* Therefore, one may test the hypothesis that the 3D gravitating mass is distributed in the same way as the 3D stellar light,  $L_*$ , obtained from deprojecting the optical image. This “Geometric Test for Dark Matter” compares the shapes of the isopotential surfaces computed assuming  $M \propto L_*$  to the shapes of the isoemissivity surfaces of  $j_x$ , obtained from deprojecting the X-ray image.

It is important to remember that not only are the shapes of the isopotential (and therefore isoemissivity) surfaces sensitive to flattening of the gravitating mass, but they also reflect its radial distribution. This is illustrated by considering a multipole expansion of the potential for an arbitrary mass distribution of finite extent. Near the center of the mass many high-order multipole terms may contribute resulting in a highly flattened potential in that



region. As one moves away from the center the higher order terms must decay and eventually (and usually very rapidly) give way to the spherical monopole term. Hence, an ellipticity gradient in the potential, and therefore  $j_x$ , also probes the radial distribution of gravitating mass.

This Geometric Test for dark matter that is distributed differently from  $L_*$  is also a powerful test of alternative gravity theories such as MOND. The fundamental MOND equation is  $\mu\vec{g}_M = \vec{g}_N$ , where  $\vec{g}_N$  is the Newtonian force vector,  $\vec{g}_M$  is the MOND force vector, and  $\mu$  is a scalar function depending only on the ratio  $g_M/a_0$  – the magnitude of the MOND force vector over a constant. Consequently, for a given mass distribution the shapes of isopotential surfaces in MOND are the same as the shapes of isopotential surfaces in Newtonian theory. So if the Geometric Test implies dark matter using Newtonian theory it follows that dark matter is also required using the MOND theory. See Buote & Canizares (1994) for a more extensive discussion of the Geometric Test, MOND, and caveats.

The assumption of a single-phase gas for NGC 720 appears to be well justified. First, the *Chandra* spectrum (see §5) is consistent with an isothermal plasma. Second, recent observations with *Chandra* and *XMM* have found that even the gas in cooling flow groups and clusters, systems that might have been expected to be highly multiphase, is consistent with a single-phase medium (e.g., Böhringer et al. 2001; Buote et al. 2002).

There are also several lines of evidence which suggest that the approximation of hydrostatic equilibrium is a good one (see also §7.4). Although it is natural to wonder whether the gas is disturbed by tidal or ram pressure effects, it must be remembered that NGC 720 is quite isolated from other large galaxies (Dressler et al. 1986). Aside from the PA twist there are no indications of external influences in the diffuse X-ray emission; e.g., centroids computed for the elliptical apertures in §3.2.2 are all consistent within  $3'' - 4''$ .

We should also emphasize that the wiggles and other irregular features displayed by the smoothed X-ray isophotes in Figure 1 are not statistically significant and thus do not necessarily imply departures of the gas from hydrostatic equilibrium. However, even if those wiggles do in fact arise from real non-equilibrium motions in the gas, the hydrostatic assumption is still very likely a good one. Previously, in Buote & Tsai (1995) we analyzed the X-ray isophotes of a galaxy cluster formed in an N-body / hydrodynamical simulation. It was found that relatively soon after major mergers (i.e., 1-2 crossing times) the cluster settled down to a quasi-relaxed state where the hot gas traced approximately the shape of the gravitational potential even though the shapes of the X-ray isophotes displayed prominent irregular features.

As in our previous studies we shall assume negligible rotation of the hot gas. We expect this to be a good approximation for several reasons. Most importantly, like most massive elliptical galaxies there is negligible stellar rotation; NGC 720 has a mass-weighted stellar rotational velocity of  $35 \text{ km s}^{-1}$  (Busarello et al. 1992) and  $v/\sigma^* = 0.15$  (Fried & Illingworth 1994). And since much, perhaps most, of the hot gas is produced by stellar mass loss (Mathews 1990), the hot gas should also rotate negligibly. In principle, if the hot gas flows inwards while

conserving angular momentum then the resulting spin-up could translate into dynamically important rotational velocities. (This would also apply to any primordial gas flowing in from large radius.) Both theory and the observed lack of highly flattened X-ray images of galaxies and centrally E-dominated groups indicate that it is highly unlikely that angular momentum is conserved in the hot gas (Nulsen et al. 1984; Brighenti & Mathews 2000). At any rate, the lack of evidence for cooling flows noted above argues against inflowing gas. It would also be difficult to reconcile the X-ray PA twist in NGC 720 with substantial solid body rotation around a single symmetry axis. Thus, all evidence suggests negligible rotation of the hot gas.

Finally, we shall neglect the self-gravity of the hot gas in our calculations. We have shown previously using *ROSAT* data (Buote & Canizares 1994) that the mass of the hot gas is  $\lesssim 1\%$  of the gravitating mass over the entire region studied.

#### 4.2. Current Objective and Implementation

The X-ray PA twist provides immediate geometric evidence for dark matter since the stellar isophotes do not display any substantial twist. However, following our discussion in §3.2.2 regarding the removal and replacement of point sources on the derived PA values, here we investigate whether the ellipticities and radial profile of the X-ray image corroborate the evidence for dark matter provided by the PA twist. We will focus our analysis of  $\epsilon_x$  in the region  $35'' \leq a \leq 139''$ . The lower limit is chosen to avoid residual point source-replacement issues (§3.1). The upper limit avoids the outer low-surface brightness regions where  $\epsilon_x$  and PA diverge from their values at smaller  $a$ . (The origin of this divergence is unclear. Some possibilities are discussed in §7.) Since  $\Sigma_x(r)$  is quite insensitive to residual source-replacement issues and small variations in  $\epsilon_x$  and PA, we will use its constraints over the entire range  $r \leq 185''$ .

The first ingredient required for the Geometric Test is  $\Phi_*$ , the potential computed assuming  $M \propto L_*$ . Using the effective radius of  $R_e = 52''$  obtained from optical surface photometry of NGC 720 (Burstein et al. 1987), we adopt a corresponding effective semi-major axis,  $a_e = R_e/\sqrt{1 - \langle\epsilon_{\text{opt}}\rangle}$ , where  $\langle\epsilon_{\text{opt}}\rangle = 0.31$  is the intensity weighted radial average of the optical B-band isophotal ellipticities,  $\epsilon_{\text{opt}}$ , computed from the tables of Peletier et al. (1990) and Lauer et al. (1995) (see Figure 3). We approximate  $L_*$  with a spheroidal Hernquist model (Hernquist 1990, 1992) with scale length,  $a_* = a_e/1.8153 = 34.5''$ , and constant ellipticity,  $\epsilon_* = 0.31$ .

We will consider both oblate and prolate spheroids to bracket the range of projected ellipticities of a triaxial ellipsoid. With no loss in the robustness of the Geometric Test we shall also assume that the symmetry axis lies in the plane of the sky. According to the “X-Ray Shape Theorem” the unknown inclination angle  $i$  must be the same for  $\Phi_*$  and  $j_x$  if  $M \propto L_*$ . Since an inclined spheroid is necessarily rounder in projection than when viewed edge-on, deprojection assuming  $i = 90^\circ$  will yield  $\Phi_*$  and  $j_x$  with rounder shapes than in actuality. This effect tends to smear out differences in the shapes of  $\Phi_*$  and  $j_x$  and therefore makes it harder to falsify the  $M \propto L_*$  hypothesis; i.e., the assumption of  $i = 90^\circ$  is conservative in this

context.

After calculating  $\Phi_*$  the next step is to compare the shapes of the isopotential surfaces to the shapes of the isoemissivity surfaces of  $j_x$ . To perform this comparison, we parameterize  $j_x$  with a  $\beta$  model<sup>8</sup> along the major axis,  $z$  (i.e., the long axis in the sky plane):  $j_x(0, 0, z) \propto (r_c^2 + z^2)^{-3\beta}$  where  $r_c$  is the “core radius”. If  $r_c$  and  $\beta$  are given, then any  $j_x(x, y, z)$  can be computed by identifying the surfaces of constant  $j_x$  with those of  $\Phi_*$ ; i.e., for any point  $(x, y, z)$  we find the corresponding value  $Z$  such that  $\Phi_*(x, y, z) = \Phi_*(0, 0, Z)$ . Then we set  $j_x(x, y, z) = j_x(0, 0, Z)$  at which point we add a “\*” to  $j_x$  (i.e.,  $j_x^*$ ) to emphasize that its isoemissivity surfaces have been aligned with  $\Phi_*$ .

We obtain the appropriate values of  $r_c$  and  $\beta$  by projecting  $j_x^*$  along the line of sight to obtain  $\Sigma_x^*$ . Then we compute  $\Sigma_x^*(r)$  for this  $M \propto L_*$  model analogously to the *Chandra* data and perform a  $\chi^2$  fit to the data. Interestingly, this flattened  $\beta$  model is a slightly better fit ( $\chi^2 = 33.9$ ) than the spherical version reported in §3.3. The best-fitting parameters and  $1\sigma$  errors are,  $r_c = 5.3'' \pm 0.3''$  and  $\beta = 0.414 \pm 0.002$ . These  $1\sigma$  errors are computed using a Monte Carlo procedure. We randomize the best-fitting  $\Sigma_x^*(r)$  according to Gaussian statistics and fit the model as described above. After twenty such realizations are performed we compute the standard deviations of  $r_c$  and  $\beta$  obtained from the 20 runs. We take these standard deviations to be the  $1\sigma$  errors.

The X-ray image ellipticities for this  $M \propto L_*$  model, denoted by  $\epsilon_x^*$ , are also computed from  $\Sigma_x^*$  analogously to the *Chandra* data. We also compute the  $1\sigma$  errors on  $\epsilon_x^*$  using the 20 Monte Carlo runs mentioned above. For the oblate  $M \propto L_*$  model we plot  $\epsilon_x^*$  and the  $1\sigma$  errors in Figure 3 indicated by the “ $M \propto L_{\text{stars}}$  Prediction”. For most values of  $a$  the  $1\sigma$  errors are smaller than the size of the value marker.

Overall the values of  $\epsilon_x^*$  are smaller than observed. For  $a \lesssim 50''$ ,  $\epsilon_x^*$  usually lies within the error bars estimated for  $\epsilon_x$  computed from the *Chandra* image. For larger values of  $a$ ,  $\epsilon_x^*$  increasingly deviates from the observed  $\epsilon_x$  values; i.e., the deviation of  $M \propto L_*$  prediction from the observations becomes pronounced outside of  $\sim R_e$ . The primary reason why the  $M \propto L_*$  model cannot produce the X-ray ellipticities is because  $L_*$  is too centrally concentrated. Consequently, the spherically symmetric monopole term dominates the stellar potential and predicts values of  $\epsilon_x$  that are smaller than observed, particularly for  $a \gtrsim 60''$ . (Note the downturn in  $\epsilon_x^*$  at small  $a$  is an artifact of the iterative moment method used to calculate the ellipticities. The isophotal ellipticities of the  $M \propto L_*$  model continue to increase toward the center.)

To quantify the significance of this deviation between  $\epsilon_x^*$  and  $\epsilon_x$  we perform a  $\chi^2$  test defined in the usual way,

$$\chi^2 \equiv \sum_i \frac{[(\epsilon_x^*)_i - (\epsilon_x)_i]^2}{(\sigma_x^*)_i^2 + (\sigma_x)_i^2}, \quad (1)$$

where  $i$  represents each value of  $a$  included in the sum,  $\sigma_x^*$  is the standard deviation for  $\epsilon_x^*$  mentioned above, and  $\sigma_x$  is the standard deviation associated with  $\epsilon_x$  (§3.2.1). But since values (and standard deviations) of  $\epsilon_x^*$  and  $\epsilon_x$  for a

particular  $a$  are correlated with values at adjacent inner  $a$ , we cannot interpret the result with the standard  $\chi^2$  null hypothesis probability which assumes uncorrelated errors for each point.

Consequently, we construct our own  $\chi^2$  probability function that accounts for the special correlations associated with our analysis. To do this we compute  $\chi^2$  in a world where  $\Sigma_x^*$  is the real X-ray image of NGC 720. That is, starting with  $\Sigma_x^*$  generated using the best fitting values  $r_c$  and  $\beta$  we compute  $\epsilon_x^*$ ; these are just the best-fitting values  $(\epsilon_x^*)_i$  shown in Figure 3. Then we follow the same procedure used to compute the uncertainties on  $\epsilon_x$  from the real data (§3.2.1); i.e., the model counts in each  $\Sigma_x^*$  image pixel are randomized assuming poisson statistics, and then  $\epsilon_x^*$  is computed in the same manner as above. Hence, for each Monte Carlo realization of  $\Sigma_x^*$  we obtain ellipticities  $(\epsilon_x^*)_i^j$ , where  $i$  indicates the value of  $a$  and  $j$  indicates the particular realization.

We perform  $10^4$  such Monte Carlo realizations. Using all of these runs we compute the standard deviations for each  $(\epsilon_x^*)_i$ . (The magnitudes of these  $1\sigma$  errors are very similar to those obtained for the actual data shown in Figure 3.) Now for each realization  $j$  we calculate  $(\chi^2)_j$  replacing  $(\epsilon_x)_i$  and  $(\sigma_x)_i$  in equation (1) with respectively  $(\epsilon_x^*)_i^j$  and their associated standard deviations. This set of  $10^4$  values of  $(\chi^2)_j$  defines the special  $\chi^2$  probability distribution.

#### 4.3. Results

The  $\chi^2$  test reveals that the oblate  $M \propto L_*$  model is inconsistent with  $\epsilon_x$  and  $\Sigma_x(r)$  computed from the *Chandra* image at the 96% confidence level. The prolate  $M \propto L_*$  model is inconsistent at the 98% confidence level. These results correspond to  $\epsilon_x$  values computed within the region  $35'' \leq a \leq 139''$  as noted at the beginning of this section. Since the deviation between the  $M \propto L_*$  model and data increases with  $a$  (Figure 3), the significance of the discrepancy increases if we exclude data at smaller  $a$ ; e.g., if we consider instead  $\epsilon_x$  values computed within the region  $66'' \leq a \leq 139''$ , the oblate (prolate)  $M \propto L_*$  model is inconsistent with the *Chandra* data at the 98% (99%) confidence level. (If all  $\epsilon_x$  values computed within  $a = 185''$  are used then the magnitude of the discrepancy is  $> 99.99\%$  for both oblate and prolate models.)

Thus, using only the ellipticities to quantify a discrepancy, the Geometric Test demonstrates that the  $M \propto L_*$  hypothesis is unsatisfactory and that dark matter is required – independent of the temperature profile of the hot gas. This corroborates the evidence for dark matter provided by the PA twist. As discussed above, such “Geometric” evidence for dark matter cannot be explained by general modified gravity theories such as MOND.

## 5. TEMPERATURE PROFILE

Unlike the Geometric Test, to construct detailed models of the gravitating matter distribution we must have some knowledge of the temperature profile of the gas. We extracted the ACIS spectra in three circular annuli containing  $\approx 3000$  background-subtracted counts over 0.3-3 keV:  $0'' - 30''$ ,  $30'' - 70''$ , and  $70'' - 140''$ . We fit these

<sup>8</sup> Here the  $\beta$  model is used only as a convenient and accurate parameterization of  $\Sigma_x(r)$ . We do not attribute the physical significance to the model (or make many of the assumptions) that inspired its creation by Cavaliere & Fusco-Femiano (1978).



spectra with an APEC thermal plasma<sup>9</sup> modified by Galactic absorption ( $N_{\text{H}}^{\text{Gal}} = 1.55 \times 10^{20} \text{ cm}^{-2}$ ). The spectral fitting was performed with XSPEC v11.1.0v (Arnaud 1996).

Attempts to fit this model to the 0.3-3 keV data were unsuccessful for two reasons. First, below  $\sim 0.5$  keV the data lie well below the model and can only be reproduced if absorption column densities of  $N_{\text{H}}^{\text{Gal}} \approx 10 \times 10^{20} \text{ cm}^{-2}$  are fitted. This effect is undoubtedly related to existing problems in the low-energy calibration mentioned on the *Chandra* web site. We suspect that because the diffuse gas of NGC 720 has a relatively low temperature ( $\sim 0.6$  keV) this calibration problem is more serious for NGC 720 than hotter systems. And it is more serious for the diffuse gas than for the harder discrete sources (see Jeltema et al. 2002).

If we exclude data below 0.7 keV then much better fits can be obtained for Galactic absorption. However, there is also excess emission above the model for energies  $\gtrsim 2$  keV. Since this excess is most pronounced in the outer annulus it is very likely associated with the background normalization. (Recall that the background varied throughout the observation – §2.) To largely avoid this excess we then excluded data above 2 keV.

Fitting the models over 0.7-2 keV yields temperatures of  $\sim 0.6$  keV in each annulus. Since, however, we have restricted the bandwidth to such a narrow region (which also does not enclose the energy corresponding to the best-fitting temperature) the constraints on the spectral model are relatively weak. In particular, the best-fitting metallicity is  $\sim 0.1Z_{\odot}$  but it is not well constrained and depends sensitively on the chosen upper limit of the bandpass. The temperatures have best-fitting values of 0.62, 0.58, and 0.62 keV respectively in the three annuli; each has  $1\sigma$  errors of  $\approx 0.1$  keV. These values are fully consistent with the *ROSAT* and *ASCA* values obtained in these regions (Buote & Canizares 1994, 1997; Buote & Fabian 1998)

Hence, the *Chandra* data confirm that the hot gas in NGC 720 is consistent with being isothermal. Given the extenuating issues mentioned above, this is the only robust conclusion we believe can be drawn from the spectrum of the diffuse gas at this time.

## 6. ELLIPTICITY OF THE DARK MATTER HALO

The Geometric Test established the need for a dark matter halo that is distributed differently from the stars. Now we wish to find the range of halo ellipticities that are consistent with the *Chandra* data. Since we are concerned primarily with the flattening of the halo we shall follow the approach adopted in §4 and consider both oblate and prolate spheroids to bracket the range of projected ellipticities of a triaxial ellipsoid. We defer consideration of the more computationally expensive triaxial models to a future study, but in §7 we discuss briefly the suitability of a previously published triaxial model for NGC 720.

### 6.1. Preliminaries

To constrain the halo ellipticities we follow the procedure outlined in our previous related studies (e.g., Buote

& Canizares 1994, 1996b, 1998a,b) based on the pioneering approach of Binney & Strimpe (1978). We solve the equation of hydrostatic equilibrium for the gas density assuming a single-phase, isothermal, ideal gas,

$$\tilde{\rho}_{\text{g}} = \exp \left[ \Gamma (\tilde{\Phi} - 1) \right], \quad (2)$$

where  $\Gamma = -\mu m_{\text{p}} \Phi(0)/k_{\text{B}}T$  and where, e.g.,  $\tilde{\rho}_{\text{g}} = \rho_{\text{g}}(\vec{x})/\rho_{\text{g}}(0)$ . The assumption of an isothermal gas is an excellent approximation for obtaining constraints on the halo ellipticity of NGC 720<sup>10</sup>. It has been shown previously by several studies (Strimpe & Binney 1979; Fabricant et al. 1984; Buote & Canizares 1994; Buote & Tsai 1995) that constraints on the ellipticity of the gravitating matter assuming an isothermal gas are very accurate even if there is a sizable temperature gradient. (This is a direct consequence of the X-ray Shape Theorem noted in §4.) In particular, for NGC 720 the *Chandra* spectral constraints (§5) indicate a temperature profile that cannot deviate substantially from isothermal. And as we have shown previously using polytropic models of the *ROSAT* PSPC data, such small deviations from isothermality have a negligible impact on the derived halo ellipticities (Buote & Canizares 1994).

A model X-ray image is created by integrating  $j_{\text{x}} = \tilde{\rho}_{\text{g}}^2$  along the line of sight. (We ignore any spatial variations in the plasma emissivity convolved with the spectral response of the ACIS-S3 detector. Since the spectral constraints indicate the gas is near isothermal such variations in the convolved plasma emissivity are unimportant for our calculations.) As in §4 we will assume the galaxy is viewed edge-on; i.e., we do not attempt to uncover the true inclination in this analysis. Because the outermost optical isophotes are quite flattened (ellipticity  $\sim 0.45$ ) it is unlikely that the symmetry axis is significantly inclined to the line of sight. For such small inclination angles the halo ellipticity deduced from the X-ray analysis assuming  $i = 90^\circ$  is a very good representation of the true value (e.g., Strimpe & Binney 1979; Buote & Tsai 1995).

For studying the ellipticity of the dark matter halo we focus our attention on models where the mass is stratified on concentric, similar spheroids (“spheroidal mass distributions”). We focus on the following density profiles having asymptotic slopes spanning the interesting range -2 to -4: (1)  $\rho \propto (a_{\text{s}}^2 + a^2)^{-1}$ , (2) NFW model,  $\rho \propto a^{-1}(a_{\text{s}} + a)^{-2}$  (Navarro et al. 1997), and (3) Hernquist model,  $\rho \propto a^{-1}(a_{\text{s}} + a)^{-3}$  (Hernquist 1990, 1992). Here  $a$  is the semi-major axis and  $a_{\text{s}}$  is a scale length. For comparison we shall also summarize results for mass distributions corresponding to potentials that are themselves stratified on concentric, similar spheroids (“spheroidal potentials”). Such potentials are generated by mass distributions whose ellipticity varies as a function of  $a$ ; e.g., the logarithmic potential,  $\Phi \propto \ln(a_{\text{s}}^2 + a^2)$ , discussed by Binney & Tremaine (1987).

Given a particular mass model we compute (1) its potential, (2)  $\rho_{\text{g}}$ , and then (3) the model X-ray image as described above. Next we compute the ellipticities and radial profile of the model image just as done for the actual

<sup>9</sup> <http://hea-www.harvard.edu/APEC/>

<sup>10</sup> In principle the method used to test the  $M \propto L_{\star}$  model in §4 can be applied to any mass model to constrain its ellipticity and scale length. This approach has the advantages of not requiring one to specify (1) the temperature profile and (2) how the gas density  $\rho_{\text{g}}$  is disentangled from  $\Sigma_{\text{x}}$ . The primary disadvantage is that the method based on the Geometric Test does not, for a general mass model, constrain the mass scale length as well as the approach adopted in this section.

*Chandra* data. We obtain the optimum model parameters by performing a  $\chi^2$  fit of the model ellipticities and radial profile to the data. The free parameters for the models are  $\epsilon$ ,  $a_s$ ,  $\Gamma$ , and the normalization of the radial profile. Here  $\epsilon$  is the ellipticity of the mass for the spheroidal mass distributions or the ellipticity of the potential for the spheroidal potentials.

We calculate errors on the model parameters using a Monte Carlo procedure similar to that done for the Geometric Test. For a given mass model (e.g., NFW) the  $\Sigma_x(r)$  and  $\epsilon_x$  values of the best-fitting model serve as the reference values. Then we randomize each of these reference values according to gaussian statistics and perform fits to these randomized values analogously to the real data. We calculate the standard deviation of the best-fitting model parameters obtained from 20 Monte Carlo runs. We take these standard deviations to be the  $1\sigma$  errors. (Note that since the value of  $\epsilon_x$  at a given  $a$  is correlated with values at adjacent inner  $a$ , this procedure slightly overestimates the errors on  $\epsilon_x$ . This primarily translates to a slight overestimate of the  $1\sigma$  errors for  $\epsilon$ .)

## 6.2. Results

In Table 1 we list best-fitting parameters and  $\chi^2$  values for the “spheroidal mass distribution” dark matter models. Technically, such single-component mass models represent the total gravitating matter (stars, gas, dark matter) in the system. However, as we discuss below, the dark matter sufficiently dominates the potential so that the models in Table 1 effectively represent the dark matter. Only  $\epsilon_x$  values for  $35'' \leq a \leq 139''$  are included in the fits for the same reasons as stated for the Geometric Test (see §4.2).

The models give consistent best-fitting values of  $\epsilon \approx 0.35 - 0.40$  with  $1\sigma$  errors of magnitude 5%-8%. The lowest ellipticity estimate is provided by the oblate  $\rho \sim a^{-2}$  model for which the  $3\sigma$  error range is  $0.27 \leq \epsilon \leq 0.45$ . The oblate NFW model provides the highest ellipticity estimate with a  $3\sigma$  error range  $0.35 \leq \epsilon \leq 0.47$ . Overall, though, there is very little difference in the fitted parameters for oblate versus prolate models.

Previously, in Buote & Canizares (1997) we presented our final analysis of the *ROSAT* PSPC data of NGC 720 and inferred  $0.44 \leq \epsilon \leq 0.68$  (90% conf.) for the  $\rho \sim a^{-2}$  model. These ellipticities are systematically higher because the point sources discovered (and removed) by *Chandra* were unresolved and therefore contaminated the PSPC analysis. However, in that same paper we also estimated the effect of such unresolved discrete sources on  $\epsilon$  by assuming the discrete sources would have the same spatial distribution as the optical light. We normalized the X-ray emission of such a model using the hard ( $T \gtrsim 5$  keV) bremsstrahlung component discovered by *ASCA*. For our maximal discrete model we obtained  $0.29 \leq \epsilon \leq 0.60$  (90% conf.) which is fully consistent with the *Chandra* values.

Recall that the average B-band isophotal ellipticity is  $\langle \epsilon_{\text{opt}} \rangle = 0.31$  which is near the  $3\sigma$  lower limit for the  $\rho \sim a^{-2}$  models. The maximum optical ellipticity of  $\approx 0.45$  (see Figure 3) is near the  $3\sigma$  upper limit for all the models in Table 1. Hence, the ellipticity of the dark matter inferred from the *Chandra* image is not very different from that of the optical light.

The  $\rho \sim a^{-2}$  model provides the best  $\chi^2$  fits, and the

quality of the fit is progressively worse for models with steeper density profiles; i.e., the Hernquist model fits even worse than the NFW model. The NFW and Hernquist models produce lower quality fits in part because they predict radially decreasing  $\epsilon_x$  profiles in contrast to the essentially constant  $\epsilon_x$  profile generated by the  $\rho \sim a^{-2}$  model which agrees better with the *Chandra* data (Figure 4). More importantly, the NFW and Hernquist models have difficulty fitting the inner bins of the radial profile. (The Hernquist model deviations from the data are similar to, but larger than, those of the NFW model shown in Figure 4.) If the 3 inner bins are excluded the NFW model fits as well, yields the same  $\epsilon$  values, and predicts essentially the same constant  $\epsilon_x$  profile, as the  $\rho \sim a^{-2}$  model. This behavior is easily understood because the best-fitting scale length,  $a_s = 42''$ , is also much larger than before which in effect flattens out the NFW density profile so that approximately  $\rho \sim a^{-2}$  over most of the image.

Let us now consider the effect of the mass associated with the visible stars on the inferred ellipticity of the dark matter. At the very least we know that the values of  $\epsilon$  in Table 1 represent lower limits for the dark matter. This is because mass distributed like the stars predicts  $\epsilon_x$  values smaller than observed (Figure 3). So if the stars make a sizable contribution to the shape of the gravitational potential, then the dark matter will have to be flatter than inferred in Table 1 to compensate for the rounder stellar potential. (Note the mass of hot gas is much less than the gravitating mass over the region being considered – see Buote & Canizares 1994).

We also know from the Geometric Test, and from the results for the Hernquist models in Table 1, that a stellar mass model is a very poor fit to the *Chandra* data. Recall from §4.2 that the stellar mass is represented by a Hernquist model with  $a_s = 34.5''$  and  $\epsilon = 0.31$ . In Table 1 we see that even the best Hernquist models provide the worst fits, and since the stellar values of  $\epsilon$  and (especially)  $a_s$  are many standard deviations away from the best-fitting values in the table, it is clear that the stellar model is a far worse fit to the data than the best  $\rho \sim a^{-2}$  model. It follows that the stars cannot make a substantial contribution to the potential defined by the models in Table 1 as we found previously when modeling the *ROSAT* PSPC data (Buote & Canizares 1994). Thus, the models in Table 1 should be associated with the dark matter.

It is interesting to consider this conclusion in the context of the mass-to-light ratio,  $M/L_B$ . For a distance of  $25h_{70}^{-1}$  Mpc the B-band luminosity of NGC 720 is  $L_B = 3.3h_{70}^{-2} \times 10^{10}L_\odot$  (Donnelly et al. 1990). Assuming a gas temperature of  $T = 0.6$  keV (§5), the best-fitting oblate  $\rho \sim a^{-2}$  dark halo model gives  $M/L_B$  values in units of  $h_{70}M_\odot/L_\odot$  of 6.0 at  $r = R_e$ , 12.3 at  $r = 2R_e$ , and 18.7 at  $r = 3R_e$ ; here the masses are spherically averaged and  $R_e = 52'' = 6.2$  kpc is the optical effective radius used to define the stellar model in §4.2. For comparison, the best-fitting oblate NFW model gives  $M/L_B$  values in solar units of 6.8 at  $r = R_e$ , 12.7 at  $r = 2R_e$ , and 17.0 at  $r = 3R_e$ .

For  $r = R_e$  these values are comparable to the value of  $M/L_B \approx 7M_\odot/L_\odot$  determined from stellar dynamical studies within  $1R_e$  (e.g., van der Marel 1991). The agreement of the X-ray and optical values lends further support

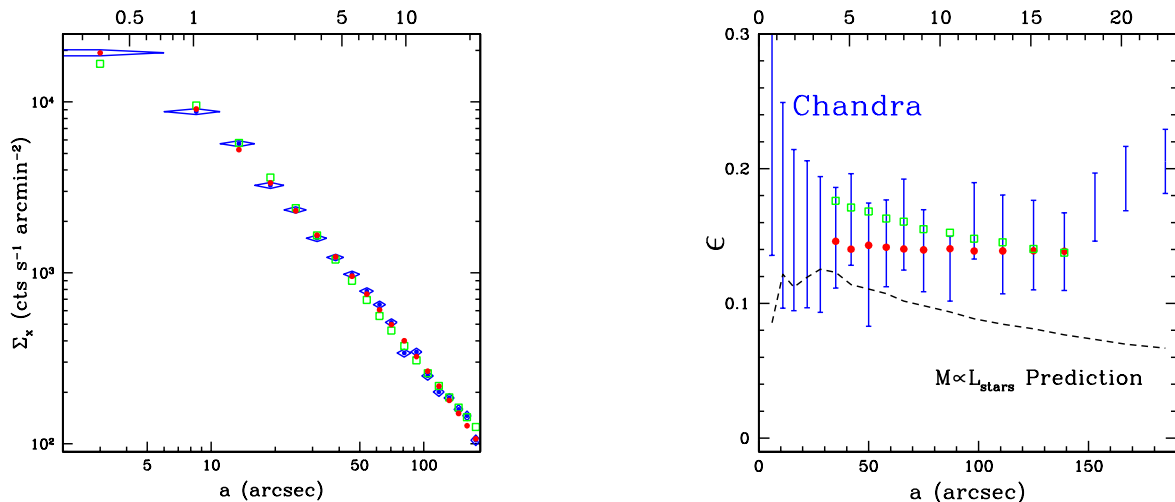


FIG. 4.— (Left panel) Radial profile denoted by diamonds (blue). Also shown are the best-fitting radial profiles generated by (oblate) DM halos corresponding to a  $\rho \sim a^{-2}$  profile (filled circles – red) and an NFW profile (open squares – green). (Right panel) X-ray ellipticities predicted by these DM models. The error bars (blue) are the values of  $\epsilon_x$  measured from the source-free *Chandra* data, and the dashed line is the prediction if mass follows the stars as in Figure 3. We express  $a$  in kpc on the top axis.

TABLE 1  
ELLIPTICITY OF THE DARK MATTER HALO

Model	Oblate				Prolate			
	$\epsilon$	$a_s$ (arcsec)	$\Gamma$	$\chi^2$	$\epsilon$	$a_s$ (arcsec)	$\Gamma$	$\chi^2$
$\rho \sim a^{-2}$	$0.37 \pm 0.03$	$1.9 \pm 0.2$	$7.95 \pm 0.05$	32.6	$0.36 \pm 0.02$	$2.1 \pm 0.2$	$7.82 \pm 0.05$	32.4
NFW	$0.41 \pm 0.02$	$26.6 \pm 0.7$	$5.95 \pm 0.03$	69.8	$0.39 \pm 0.02$	$29.3 \pm 0.6$	$5.95 \pm 0.03$	72.5
Hernquist	$0.38 \pm 0.03$	$58.0 \pm 1.2$	$5.46 \pm 0.03$	99.3	$0.36 \pm 0.02$	$63.4 \pm 1.3$	$5.49 \pm 0.03$	102.2

Note. — Best-fitting values and  $1\sigma$  errors obtained for selected dark matter halo models. The mass distributions are perfect spheroids with ellipticity denoted by  $\epsilon$ ; see §6.1 for definitions of  $a_s$  and  $\Gamma$ . There are 26 degrees of freedom associated with each fit.

to the hydrostatic equilibrium assumption. Since the X-ray ellipticities and radial profile (as mentioned above) indicate that the dark matter dominates the mass over most of the region we have studied, the agreement between the X-ray and stellar dynamical masses of NGC 720 also implies that the stellar dynamical mass estimate of NGC 720 must mostly reflect the dark matter and not simply the stellar mass.

Finally, the “spheroidal potential” models give results fully consistent with the spheroidal mass distributions. For example, for the model,  $\Phi \propto \ln(a_s^2 + a^2)$ , we obtain (for the oblate case)  $a_s = 5.2'' \pm 0.3''$ ,  $\Gamma = 5.33 \pm 0.05$ , and an ellipticity of the potential of  $0.15 \pm 0.01$ . Therefore, the best-fitting ellipticity of the dark matter is 0.20 for  $a \ll a_s$  and 0.43 for  $a \gg a_s$ ; i.e.,  $\epsilon \approx 0.35 - 0.40$  over most of the image.

## 7. CONCLUSIONS

We have analyzed a new *Chandra* ACIS-S observation of the elliptical galaxy NGC 720 to verify the existence of a dark matter halo and to measure the flattening of the dark halo. The ACIS image reveals over 60 point sources embedded in the diffuse emission from the hot gas. Most of these sources were not detected with previous X-ray observations, and analysis of their properties is presented in a separate paper (Jeltema et al. 2002). We found it

difficult to accurately replace point sources located near the center of the galaxy with local diffuse emission which hindered reliable computation of  $\epsilon_x$  and PA for  $a \lesssim 30''$ . This was not a problem for larger  $a$  where the standard CIAO software tool DMFILTH was able to accurately replace point sources with local diffuse emission.

For  $30'' \lesssim a \lesssim 150''$  the X-ray ellipticity is consistent with a constant value,  $\epsilon_x \approx 0.15$ , which is systematically less than the values 0.2-0.3 obtained from previous *ROSAT* PSPC and HRI observations. This discrepancy can be attributed directly to the unresolved point sources in the *ROSAT* observations. The magnitude of the PA twist discovered by *ROSAT* is confirmed by the *Chandra* data: PA  $\approx 110^\circ$  for  $70'' \lesssim a \lesssim 150''$  and PA  $\approx 140^\circ$  (similar to optical value) for  $a \lesssim 30''$ . However, the twist between  $a = 30'' - 60''$  is gradual in the source-free *Chandra* data in contrast to the sharp jump at  $a \approx 60''$  observed by the *ROSAT* HRI. The behavior seen by the HRI is also attributed directly to unresolved point sources.

### 7.1. Evidence for a Triaxial Dark Matter Halo

The X-ray PA twist for  $a \lesssim 150''$  provides immediate evidence for dark matter because the optical isophotes display no evidence for such a twist. (This is a consequence of the “X-ray Shape Theorem” which assumes that the hot gas is single-phase – but not necessarily isothermal –

and in hydrostatic equilibrium – see §4.) The revised PA twist also provides strong evidence that the dark matter is triaxial. Previously, Romanowsky & Kochanek (1998) constructed triaxial models of the *ROSAT* PSPC and HRI data of NGC 720. Their best model produced a PA twist of  $\sim 20^\circ$  such that  $\text{PA} \approx 140^\circ$  at the center and  $\text{PA} \approx 120^\circ$  for  $a \gtrsim 60''$ . In Romanowsky & Kochanek’s model the PA falls immediately, though gradually, from  $a = 0$  until it levels off for  $a \gtrsim 60''$ . This gradual twist disagreed strongly with the sharp jump displayed by HRI twist near  $a \approx 60''$  which the *Chandra* observation has shown to be the result of unresolved point sources in the HRI data.

Visual comparison of the *Chandra* PA twist (Figure 3) to Romanowsky & Kochanek’s best triaxial model (see their figure 7) reveals that they agree quite well for  $a \lesssim 150''$ . In fact, we expect that even better agreement would be achieved with the *Chandra* data because Romanowsky & Kochanek had to try to match the larger *ROSAT* ellipticities which inhibit the ability to produce a large PA twist – a point we originally made in Buote & Canizares (1996a) for NGC 720. Thus, the more gradual X-ray PA twist revealed by *Chandra* provides strong evidence for a triaxial dark matter halo and lends important support to the assumption of hydrostatic equilibrium for  $a \lesssim 150''$ .

### 7.2. Ellipticity of the Dark Matter

To constrain the ellipticity of the dark matter halo we considered both oblate and prolate spheroidal mass models to bracket the full range of (projected) ellipticities of a triaxial ellipsoid. Spheroidal models have the important advantage over triaxial models of being less expensive to compute.

First, to complement the evidence for dark matter provided by the PA twist, we performed a “Geometric Test for Dark Matter” to examine whether mass distributed like the stars ( $M \propto L_*$ ) can match the observed X-ray ellipticities (irrespective of the PA twist). Focusing on  $\epsilon_x$  measured for semi-major axes  $35'' \lesssim a \lesssim 139''$  we find that the  $M \propto L_*$  hypothesis is inconsistent with the *Chandra* ellipticities at the 96% confidence level for oblate models and at the 98% confidence level for prolate models. *Thus, both the PA twist and the ellipticities of the Chandra image imply the existence of dark matter independent of the temperature profile of the gas. This evidence for dark matter cannot be explained by general modified gravity theories such as MOND.*

Second, for an assumed spheroidal model of the dark matter we generated a model X-ray image to compare the model ellipticities and radial profile to the *Chandra* data. The dark matter density model,  $\rho \propto (a_s^2 + a^2)^{-1}$ , provides the best fit to the data and gives ellipticities and  $1\sigma$  errors of  $\epsilon = 0.37 \pm 0.03$  (oblate) and  $\epsilon = 0.36 \pm 0.02$  (prolate). NFW and Hernquist models give similar ellipticities for the dark matter. These ellipticities are less than the values of 0.44–0.68 (90% conf.) obtained from our previous *ROSAT* observations which did not account for unresolved point sources. In our previous *ROSAT* and *ASCA* analysis of NGC 720 which did attempt to account for unresolved point sources assuming such sources follow the stellar light (Buote & Canizares 1997), we obtained  $0.29 \leq \epsilon \leq 0.60$  (90% conf.) which is fully consistent with the (source-free) *Chandra* values. It follows that unresolved sources

remaining in the *Chandra* image should have a negligible impact on the dark matter ellipticities determined in this paper. (This conclusion can be checked directly with a deeper *Chandra* observation so that point sources can be detected to a lower flux limit.)

The ellipticity of the dark matter inferred from the *Chandra* data is not very different from the optical light,  $\langle \epsilon_{\text{opt}} \rangle = 0.31$  and  $\epsilon_{\text{opt}}^{\text{max}} \approx 0.45$ . But this does not contradict the results from the Geometric Test. The primary reason why the  $M \propto L_*$  model cannot produce the X-ray ellipticities is because  $L_*$  is too centrally concentrated. Consequently, the spherically symmetric monopole term dominates the stellar potential and predicts values of  $\epsilon_x$  that are smaller than observed, particularly for  $a \gtrsim 60''$ .

The NFW and Hernquist mass models do not fit nearly as well as the  $\rho \sim a^{-2}$  model, this discrepancy primarily arising from the radial profile in the inner regions. If the three inner bins are excluded from the fits (i.e.,  $a \leq 16''$ ) then the NFW model fits as well as the  $\rho \sim a^{-2}$  model. But the resulting larger scale-length of the NFW model implies that the NFW density behaves approximately as  $\rho \sim a^{-2}$  over the  $a$  range fitted. So unless the mass actually consists of two components, i.e., “something” plus NFW, the  $\rho \sim a^{-2}$  model is clearly favored. This “something” would have to be more centrally concentrated than the optical light (which follows an  $R^{1/4}$  law with  $R_e = 52''$ ).

### 7.3. Strange Behavior at Large Radius

At large radius ( $150'' \lesssim a \lesssim 180''$ )  $\epsilon_x$  increases steadily to a value of  $\approx 0.20$  while the position angle decreases to a value of  $\approx 80^\circ$ . These changes are highly statistically significant, although (1) the fact that this region is near the edge of the CCD, and (2) the PAs measured by *ROSAT* and *Chandra* in this region do not agree, suggest that an independent observation with the wide-field CCDs on *XMM* should be used to verify the results in this region.

If the *Chandra* values for  $\epsilon_x$  and PA are correct in this region, then a physical interpretation is necessary. We have argued that there are several good reasons to expect that the hot gas is in hydrostatic equilibrium (see below). However, it is possible that the hydrostatic assumption is valid only for  $a \lesssim 150''$  where the PA twist is consistent with the triaxial dark matter halo of Romanowsky & Kochanek (1998); i.e., the divergence in PA for larger  $a$  could signal the departure from hydrostatic equilibrium.

If the hydrostatic condition does hold for  $a \gtrsim 150''$  then there must be another, larger scale, component in the dark matter. The possibility of large-scale dark matter in NGC 720 has been suggested from analysis of its dwarf satellites by Dressler et al. (1986). Why such a separate dark component decides to assert itself at  $a \approx 150''$  is unclear.

### 7.4. Hydrostatic Equilibrium vs. Merger

Since the evidence for dark matter in NGC 720 provided by the *Chandra* data rests primarily on the assumption that the hot gas is in hydrostatic equilibrium, here we summarize the arguments in favor of equilibrium: (1) external influences on the diffuse gas should be negligible because NGC 720 is very isolated (§4.1), (2) other than the PA twisting, there are no notable asymmetries in the X-ray isophotes – in particular no substantial centroid shifts

(§4.1), (3) an N-body / hydrodynamical simulation suggests for a system without obvious subclustering the X-ray shape analysis should be valid (§4.1), (4) evidence for dark matter is provided separately by  $\epsilon_x$  and PA (§7.1 and §7.2), (5) Romanowsky & Kochanek triaxial model explains PA twist within  $a \sim 150''$  (§7.1), and (6) the gravitating mass within  $1R_e$  determined from X-rays agrees with the stellar dynamical value (§6.2).

A final argument for equilibrium, at least in the central regions, is provided by the ages of the stars. Terlevich & Forbes (2002) estimate a relatively young age of 3-4 Gyr for the central stellar population in NGC 720, consistent with a fairly recent merger with a gas-rich neighbor. However, the sound crossing time of the hot gas in NGC 720 is only  $\approx 0.1$  Gyr indicating that the gas has had ample time to settle down since the starburst. (Also, in the optical NGC 720 is classified as a “core galaxy” (Lauer et al. 1995) and has rounder isophotes near the center suggesting that it has not been dynamically disturbed in a long time according to the simulations of Ryden & Tinker (2002).) We conclude that for  $a \lesssim 150''$  ( $18.2h_{70}^{-1}$  kpc) that hydrostatic equilibrium is very likely to hold sufficiently well for analysis of its gravitating matter distribution.

The only evidence that may suggest a recent merger is associated with properties at large radius. First, the PA twist at large radius ( $a \gtrsim 150''$ ) cannot be explained by a single triaxial ellipsoid in hydrostatic equilibrium (§7.3). Second, the “arc” of point sources at  $a \sim 120''$  in NGC 720 discussed by Jeltema et al. (2002) is similar to shells seen in some elliptical galaxies which are thought to be merger remnants.

### 7.5. Implications for Galaxy Formation and Cosmology

The existence of dark matter in isolated elliptical galaxies has been assumed by the standard Cold Dark Matter (CDM) paradigm for many years, but primarily because of the ambiguities associated with the analysis of stellar velocities, definitive evidence for dark matter has been lacking. The *Chandra* observation of NGC 720 provides vital evidence that dark matter does indeed exist in an isolated

elliptical galaxy. This geometric evidence for dark matter is apparently the first dynamical tracer in any stellar system that has successfully distinguished dark matter from MOND (cf. Sellwood & Kosowsky 2002a).

The evidence for flattened dark matter provided by the ellipticities of the *Chandra* X-ray image of NGC 720 is inconsistent with the Self-Interacting Dark Matter (SIDM) model of Spergel & Steinhardt (2000). The SIDM model predicts that the dark matter halo should be spherical within a radius of  $\sim 10$  kpc in NGC 720 using the “collisional radius” defined by Miralda-Escudé (2002). On the other hand, the moderate flattening of the dark matter halo in NGC 720 is inconsistent with the highly flattened distributions predicted by the cold molecular dark matter model (Pfenniger et al. 1994).

The inferred ellipticity  $\epsilon \approx 0.35 - 0.4$  of the dark matter halo of NGC 720 is consistent with simulations of galaxy-scale halos in a  $\Lambda$ CDM model, but may be larger than indicated by a  $\Lambda$ WDM (i.e., “warm” dark matter) model (Bullock 2002). These ellipticities also are similar to the small number of measurements that have been made in other types of galaxies using different methods (e.g., Merrifield 2002). Finally, the evidence for triaxiality provided by the X-ray PA twist is another important verification of CDM models (e.g., Bullock 2002).

Although the *Chandra* observation of NGC 720 has provided important evidence for flattened, triaxial dark matter in an elliptical galaxy, it is essential to apply this analysis of X-ray shapes to other galaxies (and groups and clusters) to determine whether the conclusions drawn from NGC 720 are representative of other systems. Given the importance of detecting and removing point sources for the analysis of dark matter in NGC 720, it is clear that *Chandra* and its  $\approx 1''$  resolution will be essential for such studies of other galaxies.

We thank M. Krauss for helpful discussions regarding the features in the ACIS-S exposure map, and J. Sellwood and the anonymous referee for comments on the manuscript. TEJ was supported by an NSF fellowship.

## REFERENCES

- Arnaud, K. A. 1996, in ASP Conf. Ser. 101: Astronomical Data Analysis Software and Systems V, Vol. 5, 17
- Böhringer, H., Belsole, E., Kennea, J., Matsushita, K., Molendi, S., Worrall, D. M., Mushotzky, R. F., Ehle, M., Guainazzi, M., Sakelliou, I., Stewart, G., Vestrand, W. T., & Dos Santos, S. 2001, *A&A*, 365, L181
- Baes, M. & Dejonghe, H. 2001, *ApJ*, 563, L19
- Binney, J. & Strimpe, O. 1978, *MNRAS*, 185, 473
- Binney, J. & Tremaine, S. 1987, *Galactic dynamics* (Princeton, NJ, Princeton University Press, 1987, 747 p.)
- Brighenti, F. & Mathews, W. G. 2000, *ApJ*, 539, 675
- Bullock, J. S. 2002, in May 2001 Yale workshop The Shapes of Galaxies and their Halos, in press (astro-ph/0106380)
- Buote, D. A. & Canizares, C. R. 1994, *ApJ*, 427, 86
- . 1996a, *ApJ*, 468, 184
- . 1996b, *ApJ*, 457, 177
- . 1997, *ApJ*, 474, 650
- Buote, D. A. & Canizares, C. R. 1998a, in ASP Conf. Ser. 136: Galactic Halos, 289-298
- . 1998b, *MNRAS*, 298, 811
- Buote, D. A. & Fabian, A. C. 1998, *MNRAS*, 296, 977
- Buote, D. A., Lewis, A. D., Brighenti, F., & Mathews, W. G. 2002, *ApJ*, submitted (astro-ph/0205362)
- Buote, D. A. & Tsai, J. C. 1995, *ApJ*, 439, 29
- Burstein, D., Davies, R. L., Dressler, A., Faber, S. M., Stone, R. P. S., Lynden-Bell, D., Terlevich, R. J., & Wegner, G. 1987, *ApJS*, 64, 601
- Busarello, G., Longo, G., & Feoli, A. 1992, *A&A*, 262, 52
- Carter, D. & Metcalfe, N. 1980, *MNRAS*, 191, 325
- Cavaliere, A. & Fusco-Femiano, R. 1978, *A&A*, 70, 677
- Davis, J. E. 2001, *ApJ*, 548, 1010
- de Zeeuw, P. T. 1997, in ASP Conf. Ser. 116: The Nature of Elliptical Galaxies; 2nd Stromlo Symposium, 44
- Donnelly, R. H., Faber, S. M., & O’Connell, R. M. 1990, *ApJ*, 354, 52
- Dressler, A., Schechter, P. L., & Rose, J. A. 1986, *AJ*, 91, 1058
- Evans, N. W. 2002, in IDM 2000: Third International Workshop on the Identification of Dark Matter”, ed. N. Spooner (World Scientific), in press (astro-ph/0102082)
- Fabbiano, G. 1989, *ARA&A*, 27, 87
- Fabricant, D., Rybicki, G., & Gorenstein, P. 1984, *ApJ*, 286, 186
- Fried, J. W. & Illingworth, G. D. 1994, *AJ*, 107, 992
- Gerhard, O. 2002, in The Mass of Galaxies at Low and High Redshift, eds. R. Bender and A. Renzini, ESO Astrophysics Symposia, in press (astro-ph/0203108)
- Hernquist, L. 1990, *ApJ*, 356, 359
- . 1992, *ApJ*, 400, 460
- Jeltema, T. E., Canizares, C. R., Buote, D. A., & Garmire, G. P. 2002, *ApJ*, submitted

- Jones, C., Stern, C., Forman, W., Breen, J., David, L., Tucker, W., & Franx, M. 1997, *ApJ*, 482, 143
- Keeton, C. R., Kochanek, C. S., & Falco, E. E. 1998, *ApJ*, 509, 561
- Lauer, T. R., Ajhar, E. A., Byun, Y.-I., Dressler, A., Faber, S. M., Grillmair, C., Kormendy, J., Richstone, D., & Tremaine, S. 1995, *AJ*, 110, 2622
- Mathews, W. G. 1990, *ApJ*, 354, 468
- Merrifield, M. R. 2002, in May 2001 Yale workshop The Shapes of Galaxies and their Halos, in press (astro-ph/0107291)
- Milgrom, M. 1983a, *ApJ*, 270, 371
- . 1983b, *ApJ*, 270, 384
- . 1983c, *ApJ*, 270, 365
- Miralda-Escudé, J. 2002, *ApJ*, 564, 60
- Natarajan, P. & Refregier, A. 2000, *ApJ*, 538, L113
- Navarro, J. F., Frenk, C. S., & White, S. D. M. 1997, *ApJ*, 490, 493
- Nulsen, P. E. J. & Bohringer, H. 1995, *MNRAS*, 274, 1093
- Nulsen, P. E. J., Stewart, G. C., & Fabian, A. C. 1984, *MNRAS*, 208, 185
- Peletier, R. F., Davies, R. L., Illingworth, G. D., Davis, L. E., & Cawson, M. 1990, *AJ*, 100, 1091
- Pfenniger, D., Combes, F., & Martinet, L. 1994, *A&A*, 285, 79
- Rees, M. 2000, *New perspectives in astrophysical cosmology* (Cambridge, U.K. ; New York : Cambridge University Press.)
- Romanowsky, A. J. & Kochanek, C. S. 1998, *ApJ*, 493, 641
- Ryden, B. G. & Tinker, J. 2002, in *The Shapes of Galaxies and Their Halos*, proceedings of the Yale Cosmology Workshop, in press (astro-ph/0106500)
- Sackett, P. D. 1996, in *IAU Symp. 173: Astrophysical Applications of Gravitational Lensing*, Vol. 173, 165
- Sarazin, C. L., Irwin, J. A., & Bregman, J. N. 2000, *ApJ*, 544, L101
- Sellwood, J. A. & Kosowsky, A. 2002a, in *The Dynamics, Structure and History of Galaxies* (eds. G. S. Da Costa and E. M. Sadler), in press (astro-ph/0109555)
- . 2002b, in *Gas and Galaxy Evolution*, ASP Conf. Ser. (eds. J. E. Hibbard, M. P. Rupen, and J. H. van Gorkom), in press (astro-ph/0009074)
- Spiegel, D. N. & Steinhardt, P. J. 2000, *Physical Review Letters*, 84, 3760
- Strimpel, O. & Binney, J. 1979, *MNRAS*, 188, 883
- Terlevich, A. I. & Forbes, D. A. 2002, *MNRAS*, 330, 547
- Townsley, L. K., Broos, P. S., Nousek, J. A., & Garmire, G. P. 2002, *nuclear Instruments and Methods in Physics Research*, in press (astro-ph/0111031)
- van der Marel, R. P. 1991, *MNRAS*, 253, 710
- Zepf, S. E. 2002, in *The Shapes of Galaxies and Their Halos*, proceedings of the Yale Cosmology Workshop, in press (astro-ph/0106500)